

Article

Eu²⁺-Activated Ba_{0.5}Sr_{0.5}Al₂O₄ Phosphors for Screen Printing and Anti-Counterfeiting Flexible Film

Jiao Wu ^{1,†}, Quanxiao Liu ^{1,†}, Peng Gao ¹, Jiaqi Hu ¹, Meijuan Cao ¹, Junying Zhang ² , Wei Chen ³ , Jigang Wang ^{1,*} , Yuansheng Qi ^{1,*} and Zhenjun Li ^{4,5,*}

¹ Beijing Key Laboratory of Printing and Packaging Materials and Technology, Beijing Institute of Graphic Communication, Beijing 102600, China; wujiao20220912@163.com (J.W.); drllqx@163.com (Q.L.); gaopeng08252022@163.com (P.G.); hujiachi0312@163.com (J.H.); caomeijuan@bigc.edu.cn (M.C.)

² School of Physics, Beihang University, Beijing 100191, China; zjy@buaa.edu.cn

³ Department of Physics, The University of Texas at Arlington, Arlington, TX 76019-0059, USA; weichen@uta.edu

⁴ National Center for Nanoscience and Technology, CAS Key Laboratory of Nanophotonic Materials and Devices (Preparatory), Beijing 100190, China

⁵ The GBA Research Innovation Institute for Nanotechnology, Guangzhou 510700, China

* Correspondence: jigangwang@bigc.edu.cn (J.W.); yuansheng-q@bigc.edu.cn (Y.Q.); lizhenjun@nanoctr.cn (Z.L.)

† These authors contributed equally to this work.

Abstract: Herein, a series of Ba_{0.5}Sr_{0.5}Al₂O₄: xEu²⁺ ($x = 0.01, 0.02, 0.03, 0.04, 0.06$) nanophosphors were synthesized by a combustion method. The investigation encompassed the characterization of the phase purity, morphology, elemental composition, and photoluminescence behavior of Ba_{0.5}Sr_{0.5}Al₂O₄: xEu²⁺ nanoparticles. Under excitation by 303 nm and 365 nm ultraviolet light, the nanoparticles exhibited blue-green emission arising from the 4f⁶5d → 4f⁷ transition of Eu²⁺ ions. The optimal doping concentration was determined to be 2%. Notably, the nanoparticles demonstrated fluorescence lifetimes and quantum yields of 1010 ns ($\lambda_{ex} = 303$ nm), 112 ns ($\lambda_{ex} = 365$ nm), 10.5%, and 10.3%, respectively. Additionally, a comprehensive analysis of the band structure and electronic density of states was conducted, revealing a theoretical direct band gap of 4.05 eV for the Ba_{0.5}Sr_{0.5}Al₂O₄ host. In addition, the prepared fluorescent powder can be used to prepare fluorescent flexible films. This film does not change the characteristic emission of Eu²⁺ ions and has more stable physicochemical properties, which may be more suitable for use in harsh environments. Also, the fluorescent powder can be blended with polyacrylic acid to form colorless anti-counterfeiting ink that can be applied to banknotes as an anti-counterfeiting mark. A clover pattern was successfully printed using screen-printing technology, proving its potential application in the field of anti-counterfeiting.

Keywords: nanophosphor; Ba_{0.5}Sr_{0.5}Al₂O₄; polydimethylsiloxane; anti-counterfeiting



Citation: Wu, J.; Liu, Q.; Gao, P.; Hu, J.; Cao, M.; Zhang, J.; Chen, W.; Wang, J.; Qi, Y.; Li, Z. Eu²⁺-Activated Ba_{0.5}Sr_{0.5}Al₂O₄ Phosphors for Screen Printing and Anti-Counterfeiting Flexible Film. *Coatings* **2023**, *13*, 1247. <https://doi.org/10.3390/coatings13071247>

Academic Editor: Yuri M.

Strzhemechny

Received: 13 June 2023

Revised: 6 July 2023

Accepted: 11 July 2023

Published: 14 July 2023



Copyright: © 2023 by the authors. Licensee MDPI, Basel, Switzerland. This article is an open access article distributed under the terms and conditions of the Creative Commons Attribution (CC BY) license (<https://creativecommons.org/licenses/by/4.0/>).

1. Introduction

Nowadays, all kinds of counterfeit products, such as fake banknotes, fake drugs, and counterfeit food, have penetrated every aspect of our life, posing a great threat to our personal property and life and health as well as the reputation and profit of brand owners [1–3]. And with the development of economic globalization, the proliferation of these problematic products will also affect the image of the country's products, thus losing its advantage in international competition [4]. To maintain the healthy development of the market and the safety of people's life and property, in addition to using legal means to crack down on the production and sale of counterfeits, countries around the world have been continuously exploring various advanced anti-counterfeiting technologies [5], for example, multiple laser anti-counterfeiting, 1D barcode anti-counterfeiting, 2D barcode anti-counterfeiting, temperature change anti-counterfeiting, watermark anti-counterfeiting, fluorescent anti-counterfeiting, etc. [6–11]. Among them, fluorescent materials with rare-earth doped

inorganic substances are favored because of their photochemical stability, rich energy levels, and ability to achieve multi-color emission from UV to NIR [12–15]. For example, Xue Bai et al. prepared CaWO_4 : Yb^{3+} , Er^{3+} , Bi^{3+} photochromic phosphors showing reversible photochromic and dual-mode upconversion (UC) and downshifting (DS) luminescence properties, which have potential applications as composite anti-counterfeits and optical storage media [16]. Mengxiao Li et al. synthesized dual-mode luminescent NaYF_4 : Er , $\text{Yb}(\text{Tm})$ carbon quantum dots by a facile solvothermal method and successfully printed a variety of dual-mode fluorescent patterns using a mixture of a fluorescent material and an aqueous poly(acrylic acid) solution as a colorless anti-counterfeit ink, showing good dual-mode fluorescent properties [17].

Although these materials have achieved many remarkable results, these materials are simply phosphors or fluorescent inks, which have many problems, such as the single excitation mode, not being easy to preserve, not being recyclable, etc. [18,19]. Moreover, as the counterfeiting technology continues to iterate and update, the possibility of its being cracked or counterfeited remains high. In recent years, the application of a rare earth anti-counterfeiting film in anti-counterfeiting has become increasingly widespread. These films usually appear colorless and transparent in daylight but show specific anti-counterfeiting patterns when exposed to UV light, etc. This design combines the properties of both thin film and rare-earth light-emitting materials, enabling more advanced anti-counterfeiting. Polydimethylsiloxane (PDMS) is known for its high chemical and thermal stability, corrosion resistance, flexibility, and repeatability, and it is widely used in electronic components, sensors, fiber-optic waveguide coatings, and circuit board packaging [20–23]. The composite of rare-earth fluorescent material and PDMS elastic substrate can prepare an excellent flexible anti-counterfeiting material by combining the luminescent properties of rare-earth fluorescent material with the compressible and stretchable physical properties of PDMS.

Recently, Eu^{2+} -activated Ba/Sr-based aluminate phosphors have been extensively studied, and the phosphors have unique luminescence properties through Ba/Sr mutual substitution. Daisuke Nakauchi et al. synthesized Eu-doped $\text{Ba}_x\text{Sr}_{1-x}\text{Al}_2\text{O}_4$ ($x = 0, 0.1, 0.3$, and 0.5) single crystals by the floating zone method [24]. They investigated their scintillation properties, observing the high optical yield of Eu : $\text{Ba}_{0.5}\text{Sr}_{0.5}\text{Al}_2\text{O}_4$. Max Volhard synthesized $\text{Sr}_{0.97-x}\text{Ba}_x\text{Eu}_{0.03}\text{Al}_2\text{O}_4$ ($x = 0\text{--}0.97$) phosphor by the solid-phase reaction and studied the phase change and luminescence characteristics with the changing Ba content [25]. Marcos et al. investigated the X-ray excited optical luminescence (XEOL) properties of Eu-doped $\text{Ba}_{1-x}\text{Sr}_x\text{Al}_2\text{O}_4$ phosphors. They found that the XEOL yield was higher in the Ba-rich samples and the decay rate of long-lasting phosphorescence (LLP) was slower in the Sr-rich samples [26].

In this study, $\text{Ba}_{0.5}\text{Sr}_{0.5}\text{Al}_2\text{O}_4$: $x\text{Eu}^{2+}$ ($x = 0.01, 0.02, 0.03, 0.04, 0.06$) phosphor was synthesized by a simple combustion method. To study the optical properties of the phosphor, the synthesized samples were measured and characterized by scanning electron microscope (SEM), photoluminescence (PL), X-ray diffraction (XRD), etc. Additionally, the optimal doping concentration of Eu ion $x = 0.02$, and the optimal reaction temperature was 700 °C. Finally, fluorescent flexible films and anti-counterfeiting inks were prepared using the optimized samples, showing their potential applications in the field of anti-counterfeiting.

2. Experimental Section

2.1. Materials and Method

A series of $\text{Ba}_{0.5}\text{Sr}_{0.5}\text{Al}_2\text{O}_4$: $x\text{Eu}^{2+}$ ($x = 0.01, 0.02, 0.03, 0.04, 0.06$) samples were prepared by the combustion method. The raw materials used were BaCO_3 (purity: 99.99%), SrCO_3 (99.99%), Al_2O_3 (99.99%), Eu_2O_3 (99.99%), HNO_3 (80%), and urea (99.99%), which were all purchased from Tianjin Chemical Reagent Factory, Tianjin, China. The deionized water was homemade. All reagents were directly used as received without further purification.

2.2. Synthesis of Nanomaterials

First, appropriate amounts of HNO_3 and deionized water were added to BaCO_3 , SrCO_3 , Al_2O_3 , and Eu_2O_3 to prepare 0.2 mmol/mL of $\text{Ba}(\text{NO}_3)_2$, 0.5 mmol/mL of $\text{Sr}(\text{NO}_3)_3$, 1 mmol/mL of $\text{Al}(\text{NO}_3)_3$, and 0.1 mmol/mL of $\text{Eu}(\text{NO}_3)_2$ solutions, respectively. Then, $\text{Ba}(\text{NO}_3)_2$, $\text{Sr}(\text{NO}_3)_3$, $\text{Al}(\text{NO}_3)_3$ and $\text{Eu}(\text{NO}_3)_2$ solutions were measured in stoichiometric ratios ($0.5 - 0.5x:0.5 - 0.5x:2:x$) and placed in a crucible, then 2.2 g of urea for the combustion agent was added and mixed homogeneously, and placed in a preheated muffle furnace. After waiting 3 to 5 min, a loose white and porous solid powder is obtained. A series of samples can be obtained by adjusting the Eu ion doping concentration ($x = 0.01, 0.02, 0.03, 0.04, 0.06$) and reaction temperature (500, 600, 700, 800, 900 °C). Ultimately, the obtained samples were naturally cooled to room temperature and ground into powder for a test.

2.3. Preparation of Anti-Counterfeit Flexible Film and Ink

Polydimethylsiloxane (PDMS, Sylgard184, Dow Corning, Midland, MI, USA) was used to assemble the elastomer for $\text{Ba}_{0.5}\text{Sr}_{0.5}\text{Al}_2\text{O}_4:\text{Eu}^{2+}$. The milled phosphor was mixed with the uncured PDMS material and put into a mold, and then the molds were dried at 100 °C for 1 h to obtain the “ML” pattern composite phosphor. The final flexible, stretchable anti-counterfeit film was obtained by placing the resulting “ML” composite in an uncured PDMS matrix and curing it at 120 °C for 40 min.

The fluorescent powder was introduced into a mixed solution of ethanol and polyacrylic acid, followed by vigorous stirring. The amounts of polyacrylic acid and ethanol were adjusted to attain a viscosity suitable for screen printing, resulting in the final fluorescent ink.

2.4. Characterizations

The crystalline phases were collected on an X-ray diffraction (Rigaku D/Max-2400, Rigaku, Tokyo, Japan) with $\text{Cu K}\alpha$ radiation ($\lambda = 1.54 \text{ \AA}$), operating at 40 kV and 150 mA. The PLE and PL spectra were measured by a fluorescence spectrometer (FluoroMax-4, Horiba, Ltd., Kyoto, Japan). The morphology of phosphors was observed through scanning electron microscopy (Quanta 250 FEG, Thermo Fisher Scientific, Waltham, MA, USA). The fluorescence lifetime and quantum yield of phosphors were measured by a transient steady-state fluorescence spectrometer (FLS1000, Edinburgh Instruments, Edinburgh, UK). The UV-Vis absorption spectra were performed using a UV-3600 UV-Vis Near Infrared Spectrophotometer (Shimadzu Corporation, Kyoto, Japan). The energy-dispersive X-ray spectroscopy (EDS) spectrum was obtained with a desktop scanning electron microscope energy dispersive spectrometer (SU8020, Hitachi, Ltd., Hitachi, Japan).

2.5. Theoretical Calculations

The structural optimization and electronic structure calculations of $\text{Ba}_{0.5}\text{Sr}_{0.5}\text{Al}_2\text{O}_4$ were performed using density functional theory (DFT) based on first-principles calculations. The structure consists of a unit cell. All DFT calculations were performed using the Vienna ab initio Simulation Package (VASP) [27]. The Perdew–Burke–Ernzerhof (PBE) exchange–correlation functional and projector-augmented wave (PAW) pseudopotentials were employed for spin-polarized calculations [28–30]. During the structural optimization process, a convergence criterion of 10^{-6} eV for the total energy was set, and atomic positions were relaxed until the forces acting on each atom were less than $0.01 \text{ eV}/\text{\AA}$. Gaussian smearing with a width of 0.05 eV was used for the occupation of the electronic orbitals. A plane-wave cutoff energy of 500 eV was applied in all calculations. The Brillouin zone integration was performed using the Monkhorst–Pack (MP) special k-point mesh with a spacing of 0.03 \AA^{-1} .

3. Results and Discussion

3.1. Structure and Morphology Analysis of BSAO: Eu^{2+}

The phase composition and purity of $\text{Ba}_{0.5}\text{Sr}_{0.5}\text{Al}_2\text{O}_4$ (abbreviated as BSAO) phosphor were investigated by X-ray powder diffraction. Figure 1a shows the XRD patterns of the BSAO host and BSAO: $x\text{Eu}^{2+}$ ($x = 0, 0.01, 0.02, 0.03, 0.04, 0.06$) phosphors at a reaction temperatures of 600 °C. Most of the diffraction peaks of the samples can be indexed to the standard data of PDF#97-015-3164. However, for the BSAO sample, some byproducts can be observed, as noted by the rhombus. The impurity phase is inferred to be BaO, and the weight ratio to be approximately 0.4%, by a simple quantitative analysis, which can be almost ignored on the effect of the luminescence properties. According to the XRD standard cards, it is identified that the BSAO belongs to the $P6_3(173)$ space group of the hexagonal phase. The cell parameters $a = b = 8.972 \text{ \AA}$, $c = 8.606 \text{ \AA}$ calculated for BSAO are between BaAl_2O_4 ($a = b = 10.449 \text{ \AA}$, $c = 8.793 \text{ \AA}$) and SrAl_2O_4 (PDF#97-015-3164) [31,32]. Generally, it is reasonable to assume that the Eu^{2+} dopants tend to occupy the Sr^{2+} or Ba^{2+} sites based on similar effective ionic radii (IR) of the cation with varying coordination numbers (CNs) and valences [33–35]. Moreover, the main diffraction peak of (112) shifts toward a higher angle with the introduction of Eu ions as shown in Figure 1b. It means that the lattice parameters and the cell volume of the substituted samples will be reduced to some extent, which is in line with the shift of the diffraction peaks, which could be well accepted based on Bragg's law ($2d \sin \theta = n\lambda$) [36,37]. It confirms again that the Eu ions with smaller ionic radii are constantly replacing the potentially substitutable ions. Moreover, the presence of additional peaks at about 20° of the 2θ angle may be due to the unstable crystalline phase of the sample caused by the insufficient reaction temperature.

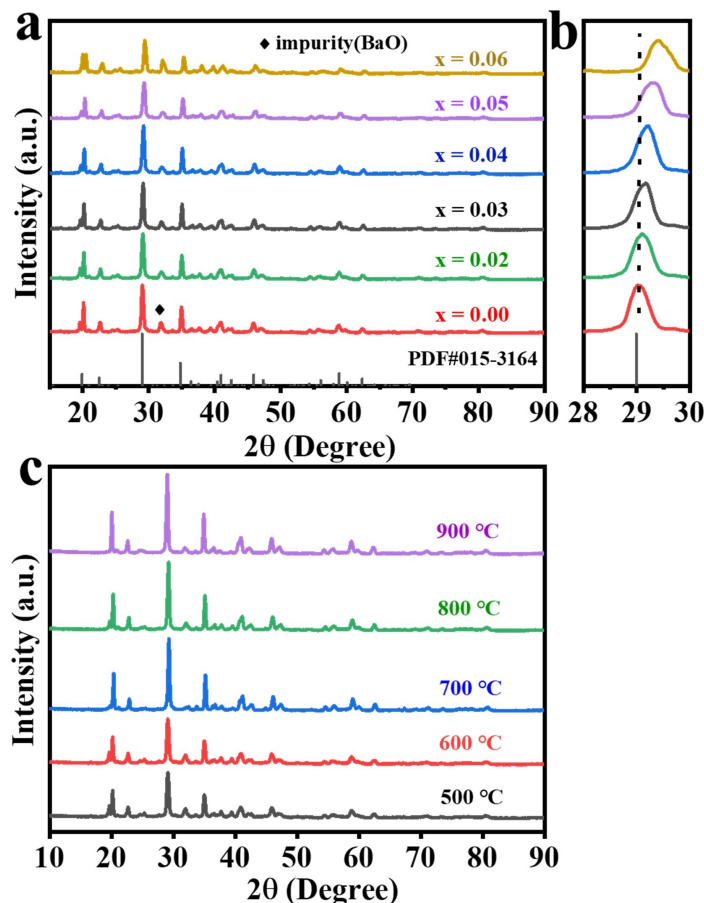


Figure 1. (a) XRD patterns of BSAO doped with different concentrations of Eu and SrAl_2O_4 standard cards; (b) the diffraction peak at (211) of BSAO: Eu^{2+} ; (c) XRD patterns of BSAO: 0.02Eu^{2+} at different reaction temperatures (500, 600, 700, 800, 900 °C).

The effect of the reaction temperature on the phase and morphology of the final sample will be further investigated. Figure 1c shows the XRD patterns of BSAO: 0.02Eu²⁺ synthesized at different reaction temperatures. With the increase in temperature, the strength of the major diffraction peak progressively grows, and the position of its diffraction peak is basically unchanged compared with Figure 1a. It means that the crystals of the BSAO: 0.02Eu²⁺ samples are formed successfully at different reaction temperatures and crystallized better with increasing temperature. In addition, the XRD pattern of the sample shows a decrease in the impurity peak when the reaction temperature is 700 °C. Furthermore, the intensity of the extra diffraction peak at the 2θ angle of about 20° gradually decreases with the increase in the reaction temperature. When the reaction temperature reaches 900 °C, the extra peaks disappear, and the crystalline phase starts to stabilize. The influence of the reaction temperature on the microscopic morphology of the phosphor is investigated using SEM pictures. Figure 2 depicts the crystal morphology of BSAO: 0.02Eu²⁺ produced at different reaction temperatures. In all five of these samples, the phosphor particles are aggregated into tiny clusters of varied shapes and sizes. In addition, there are lamellar structures with fractures and air pores. At 500–600 °C, the gaps in the sample structure progressively become smaller and gradually tend to be united, and at 700 °C, the gaps are negligible, showing a laminar structure, and the structure shows no obvious fracture symptoms. At 800–900 °C, the lamellar structure disappears gradually, and the gaps in the sample structure keep rising again, which may be caused by the violent outward burst of the gas created during the burning of the sample [38]. The irregularities in the shape, size, and pores of these samples may be related to the irregular mass flow and unequal temperature distribution of the samples during combustion [39]. Moreover, the existence of the elements Ba, Sr, Al, O, and Eu is demonstrated by the EDS spectrum of BSAO: 0.02Eu²⁺ as shown in Figure 2f. The ratio of Ba to Sr can be observed to be close to 1:1, and the successful doping of Eu ions into the host material is achieved.

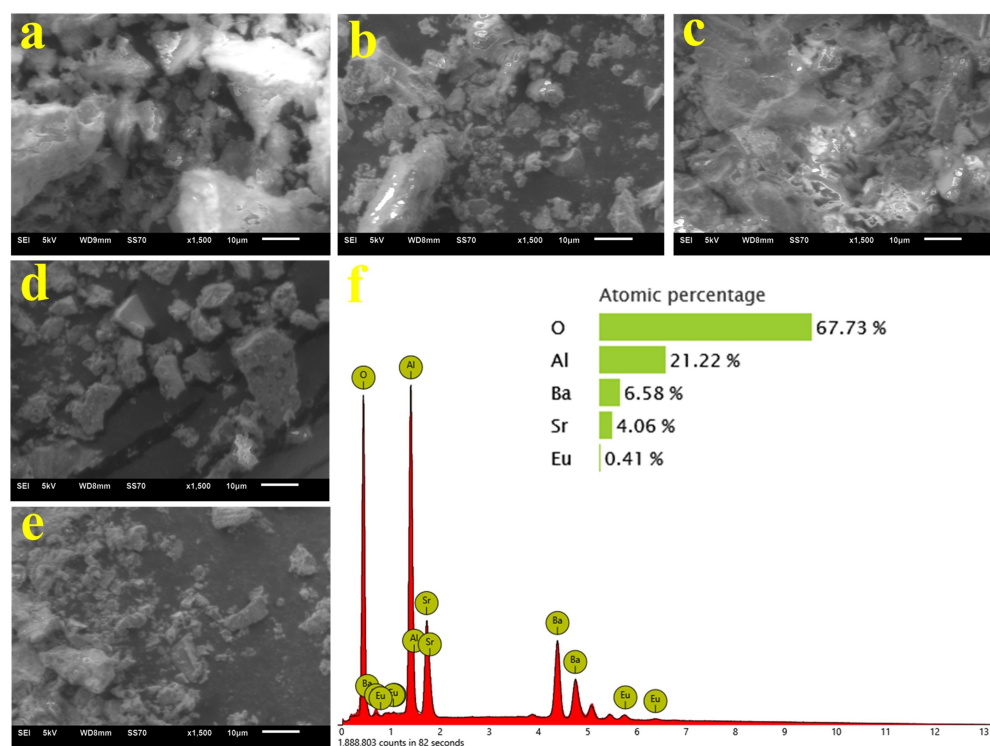


Figure 2. SEM images of BSAO: 0.02Eu²⁺ synthesized at (a–e) 500 °C–900 °C; (f) the EDS of BSAO: 0.02Eu²⁺ particles synthesized at 700 °C.

3.2. UV-Vis Absorption and Photoluminescence Properties of BSAO: Eu^{2+}

UV-vis absorption spectroscopy was used to study the absorption performance of BSAO: 0.02Eu²⁺ (Figure 3a). The absorption spectrum shows two absorption peaks from 230 to 400 nm. Absorption near 230 nm is attributed to the host band absorption. The broad absorption band covering the spectral range of 300–400 nm is assigned to the 4f→5d electronic transitions of Eu²⁺. To experimentally estimate the bandgap scale, the E_g of the BSAO: 0.02Eu²⁺ can be estimated according to the following equation [40]:

$$(\alpha h\nu)^{1/n} = A(h\nu - E_g) \quad (1)$$

where $h\nu$ is the photon energy, α is the absorption coefficient, E_g is the band gap energy (eV), and A is a constant. The value of n is determined according to the type of interband conversion. It is equal to 2 for indirect transitions and 1/2 for direct transitions [41]. In addition, the intermediate optical band gap (E_g') can be obtained by the linear fit in the flat part in Figure 3b. Then, the value of n is calculated using the following equation [42]:

$$n = \ln(\alpha h\nu) / \ln(h\nu - E_g') \quad (2)$$

As shown in Figure 3c, the value of n is approximated by 1/2. Thus, the plot of $(\alpha h\nu)^2$ versus $(h\nu - E_g)$ is shown in Figure 3d. The absorption Tauc plot shows that the band gap is 4.96 eV.

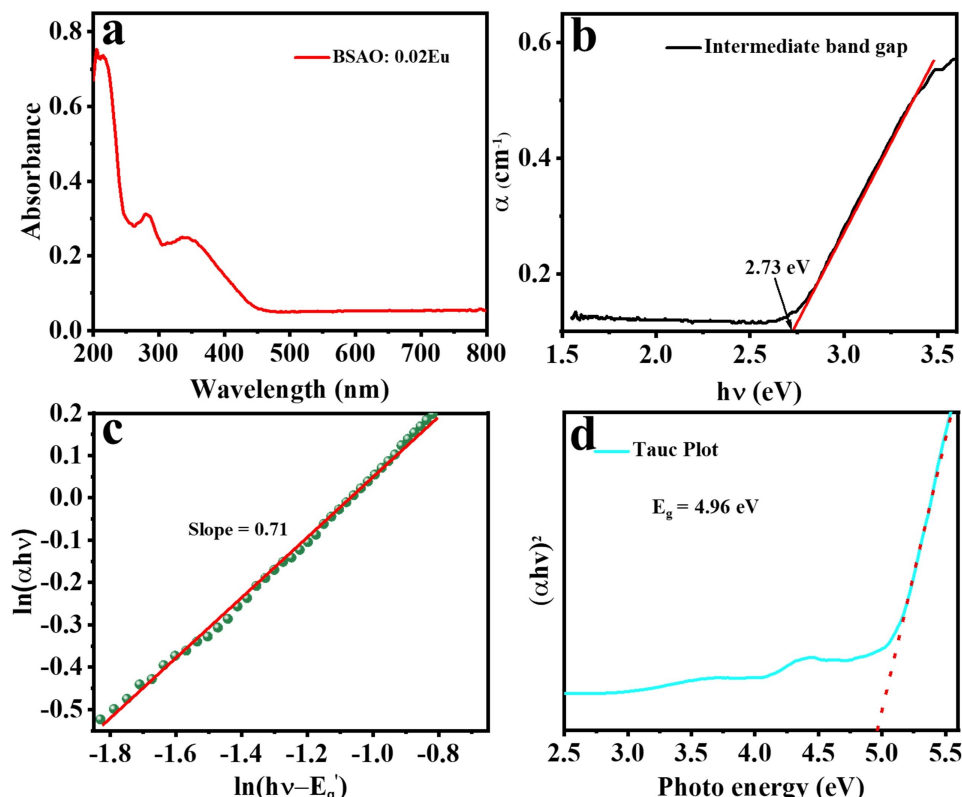


Figure 3. (a) UV-vis absorption spectra; (b) intermediate optical band gap (E_g') of BSAO: 0.02Eu²⁺; (c) graphical elaboration of Equation (2); (d) Tauc plot of absorption measurements of BSAO: 0.02Eu²⁺.

The luminescence properties of the BSAO: Eu²⁺ phosphors are investigated in detail by photoluminescence (PL) and photoluminescence excitation (PLE) spectroscopy. It is found that the peak positions and spectral shapes of emission spectra do not vary with Eu²⁺ concentration for the BSAO: Eu²⁺ nanophosphor, but the intensity of emission peaks for BSAO: $x\text{Eu}^{2+}$ ($x = 0.01, 0.02, 0.03, 0.04$, and 0.06) nanophosphor strongly depends on the doping concentration of Eu²⁺ ions. As shown in Figure 4a, the PLE spectrum of BSAO:

0.02Eu^{2+} encompasses the UV to the blue area and exhibits two broad absorption bands centered at 365 and 303 nm, which is attributable to the $4f^7 \rightarrow 4f^65d$ transition of Eu^{2+} [43]. Figure 4b,c show the emission spectra of the samples under UV excitation at 303 and 365 nm, and their emission peaks are 443 and 501 nm, respectively. The PL spectrum shows a broad asymmetric band with a maximum at 443 nm under 303 nm excitation, corresponding to the allowed $4f^65d \rightarrow 4f^7$ transition of the Eu^{2+} . As shown in Figure 4c, the narrow-band green emission, correlating to the $5d\text{-}4f$ transition of Eu^{2+} , is observed under 365 nm excitation. The full width at half-maximum (FWHM) of the emission spectrum is around 62 nm. Furthermore, concentration quenching typically occurs in the emission center when certain structural defects and nonradiative transition rates reach a saturation state. In general, the critical value of the concentration (having intense emission) is determined as the optimal doping concentration. Therefore, the strongest PL emission intensities of the BSAO: Eu^{2+} phosphors are recorded when $x = 0.02$, revealing that the optimal doping concentrations of Eu^{2+} ions in the BSAO host are 2% as illustrated in Figure 4d. Moreover, it should be clarified whether the mechanism of concentration quenching is the critical reason for their different optimal concentrations. Indeed, the energy transfer concentration quenching mechanism can be investigated by calculating the interaction coefficient (Q) as shown below [44–46]:

$$\log(I/x) = A - (Q/3) \log x \quad (3)$$

where x denotes the Eu^{2+} ion concentration, and I is the luminescence intensity. In this respect, the fitting slope ($-(Q/3)$) is determined to be -1.72 and -2.25 , respectively. The interaction coefficient (Q) values are analyzed to be about 5.16 ($\lambda_{\text{ex}} = 303$ nm) and 6.75 ($\lambda_{\text{ex}} = 365$ nm) as shown in Figure 5. All of them are close to 6, suggesting that the dipole–dipole interaction ($Q = 6$) is the main mechanism to control concentration quenching rather than the dipole–quadrupole ($Q = 8$) or quadrupole–quadrupole ($Q = 10$) interaction.

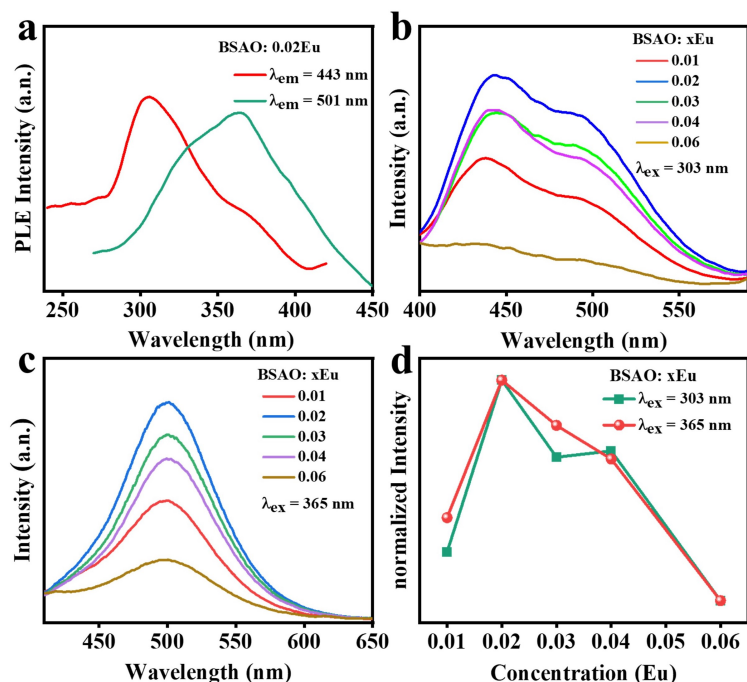


Figure 4. (a) PLE spectra of BSAO: 0.02Eu^{2+} ; PL spectra of BSAO doped with different Eu ion concentrations ($x = 0.01, 0.02, 0.03, 0.04, 0.06$) under (b) 303 nm, and (c) 365 nm; (d) Concentration dependence of the PL intensity.

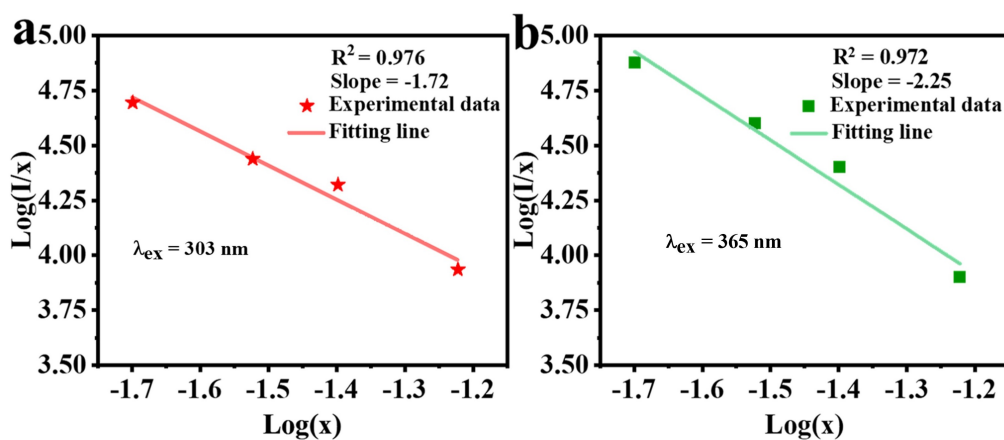


Figure 5. Linear fitting of $\log(x)$ versus $\log(I/x)$ for spectra of BSAO: 0.02Eu^{2+} phosphors. (a) $\lambda_{\text{ex}} = 303 \text{ nm}$ and (b) $\lambda_{\text{ex}} = 365 \text{ nm}$.

The reaction temperature is a highly essential aspect that directly impacts the structure and luminescent properties of the sample. The produced solutions are sintered at 500, 600, 700, 800, and 900°C , and the emission spectra of the synthesized products are given in Figure 6. When the reaction temperatures are different, the characteristics of the spectra do not change significantly under the same wavelength of excitation, except for the emission intensity. Figure 6a,b show the emission spectra of the samples under the excitation of the UV light at 303 and 365 nm. It shows a broad emission band centered at 442 and 500 nm, respectively. The luminescence intensities of the samples all reach the highest when the reaction temperature is 700°C . These blue-green emission bands are attributed to the $4f^65d \rightarrow 4f^7$ electron transition of the Eu^{2+} ion. In addition, the emission bandwidth of the samples becomes narrower when the reaction temperature is 800°C . It may be due to the improved crystallinity of the material at higher reaction temperatures, which reduces the defects and impurities that may lead to broader emission bands. Figure 6c provides a thorough illustration of this procedure.

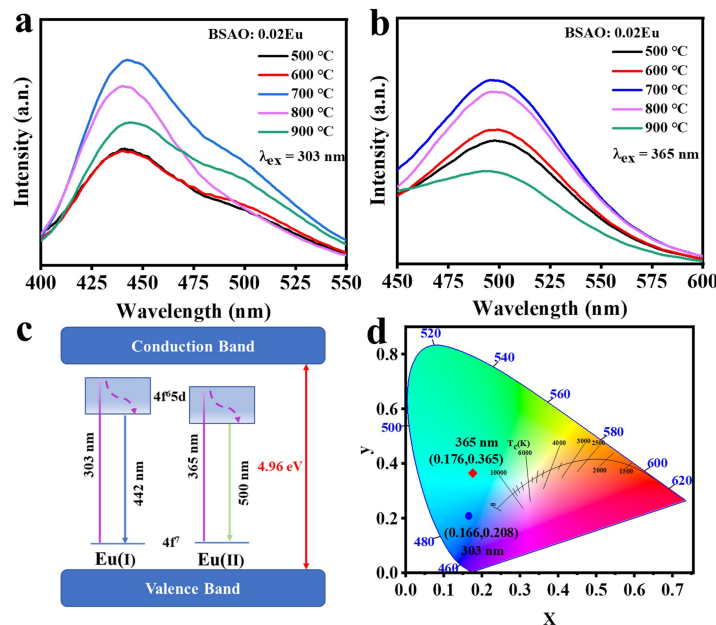


Figure 6. PL spectra of BSAO: 0.02Eu^{2+} synthesized at different reaction temperatures ($500\text{--}900^{\circ}\text{C}$) under the excitation of (a) 303 nm , (b) 365 nm ; (c) PL schematic diagram of Eu^{2+} ions in the BSAO host; (d) CIE (1931) chromaticity coordinates diagram for BSAO: 0.02Eu^{2+} under the excitation of 303 and 365 nm ultraviolet light.

Figure 6d depicts the coherent infrared energy (CIE) chromaticity coordinate positions of the BSAO: 0.02Eu²⁺ phosphor under the excitation wavelength of 303 nm and 365 nm. The corresponding CIE chromaticity coordinates are (0.166, 0.208) and (0.176, 0.365). It is observed from Figure 6d that the CIE chromaticity coordinate varies with the excitation wavelength and the corresponding colors are changed from blue to green.

Moreover, the luminescence decay curves of the BSAO: 0.02Eu²⁺ phosphor ($\lambda_{ex} = 303$ nm, $\lambda_{em} = 442$ nm; $\lambda_{ex} = 365$ nm, $\lambda_{em} = 501$ nm) are shown in Figure 7, and the decay curves are well fitted by a second-order and triple-order exponential function expressed as follows [47]:

$$I(t) = I_0 + A_1 \exp(-t/\tau_1) + A_2 \exp(-t/\tau_2) + \dots \quad (4)$$

where I_0 represents the background constant, A_1 and A_2 are constants, t is the decay time, τ_1 and τ_2 refer to the decay times of the exponential components and the average lifetimes of all BSAO with different Eu²⁺ doping concentrations are calculated by the following equation:

$$\tau^* = (A_1 \times \tau_1^2 + A_2 \times \tau_2^2 + \dots) / (A_1 \times \tau_1 + A_2 \times \tau_2 + \dots) \quad (5)$$

According to the formula, the average lifetime of BSAO: 0.02Eu²⁺ is 1010 ns ($\lambda_{ex} = 303$ nm) and 112 ns ($\lambda_{ex} = 365$ nm), respectively. Furthermore, the photoluminescence quantum yield (PLQY) is an important parameter for luminescent materials. The QY of the phosphors can usually be measured according to the percentage of the photon number emitted by the sample (ε) versus the photon number absorbed by the sample (α). The PLQY spectrum of the BSAO: 0.02Eu²⁺ phosphor is presented in Figure 7c,d. The QY can be determined by the following equation [48]:

$$PLQY = \varepsilon/\alpha = S_{em}/(S_0 - S) \quad (6)$$

where S_{em} is the integrated intensity of the emission light of the phosphor, S_0 and S is integrated with the intensity of the scattered light of the reference background plate and the phosphor, respectively. Thus, the absorbed photon number of the BSAO: 0.02Eu²⁺ phosphor is obtained by subtracting the scattered light intensity (S) of the BSAO: 0.02Eu²⁺ phosphor from the scattered light intensity (S_0) of the reference background plate. Therefore, it is clear that the QY could reach up to 10.5% ($\lambda_{ex} = 303$ nm) and 10.3% ($\lambda_{ex} = 365$ nm). The detailed parameters of the lifetimes and QY are shown in Table 1.

Table 1. Parameters of fluorescence lifetime decay curves of BSAO: 0.02Eu²⁺ and PLQY.

Excitation	PLQY	Decay Lifetimes (ns)			
		τ_1	τ_2	τ_3	τ_{avg}
303 nm	10.5% \pm 0.01%	407.71	1330.3	null	1010 \pm 0.03
365 nm	10.3% \pm 0.05%	36.94	368.6	1.4	112 \pm 0.02

3.3. Electronic Structure

The band structure and density of states (DOSs) of the BSAO host are calculated using density functional theory (DFT). Considering the mutual substitution between Ba and Sr and their atomic ratios close to 1:1 (Figure 2f), we design a structural model of Ba_{0.5}Sr_{0.5}Al₂O₄. The structural model is based on the substitution of 50% of Sr atoms with Ba in the SrAl₂O₄ system. As shown in Figure 8a,b, the valence band maximum (VBM) and the conduction band minimum (CBM) are located at the same point, indicating that BSAO exhibits a direct band gap (E_g). The predicted value of E_g is approximately 4.05 eV. In addition, as shown in Figure 8d, the experimental band gap of the BSAO host can be obtained by Equation (1). The experimental E_g (5.18 eV) is slightly larger than the calculated E_g (4.05 eV), which can be attributed to the general limitations of the generalized gradient approximation scheme in the DFT calculations [49,50]. Figure 8c displays the total density

of states (TDOS) and partial density of states (PDOS) of the BSAO host. It is observed that the d orbitals of the Ba and Sr atoms predominantly contribute to the DOS at the CBM, while the VBM is primarily derived from the p orbitals of the O atoms.

3.4. Morphology Control of BSAO: Eu^{2+} via Surfactants

Numerous factors, such as grain size, shape, and dimensionality can alter the luminescence of rare earth ions. Surfactants are extensively employed to modulate inorganic nanocrystal size, shape, and crystallinity [51]. To examine the effect of surfactants on the morphology of fluorescent materials, BSAO: 0.02 Eu^{2+} phosphors were synthesized with the assistance of surfactants. Figure 9 shows the XRD patterns of BSAO: 0.02 Eu^{2+} at a reaction temperature of 700 °C with the addition of different surfactants (polyvinyl alcohol (PVA), ethyl acetate (EA), and polyethylene glycol (PEG)). The results show that the impurity peaks decrease with the entry of the surfactant, and the position of the main diffraction peak is basically the same as that of the diffraction peak without the addition of the surfactant. In particular, the addition of PVA and PEG shows a significant reduction in the additional peaks at about 20° of the 2θ angle. Moreover, the intensity of the main diffraction peak of BSAO: 0.02 Eu^{2+} with the addition of PVA is higher, which indicates that the samples with the addition of PVA are better crystallized. Compared with the samples without the surfactant addition, the development of the samples is significantly improved. Crystals with higher crystallinity generally have fewer trapping sites and exhibit stronger luminescence. Figure 10 shows the SEM images of BSAO: 0.02 Eu^{2+} phosphor without and with different surfactants added. Figure 10b,c,d are the SEM images of the samples doped with surfactants PVA, EA, and PEG, respectively. By comparison, it is found that the samples with the addition of PVA are more compact and show an obvious lamellar structure. Therefore, adding surfactant PVA can improve the morphology of BSAO: Eu^{2+} phosphor.

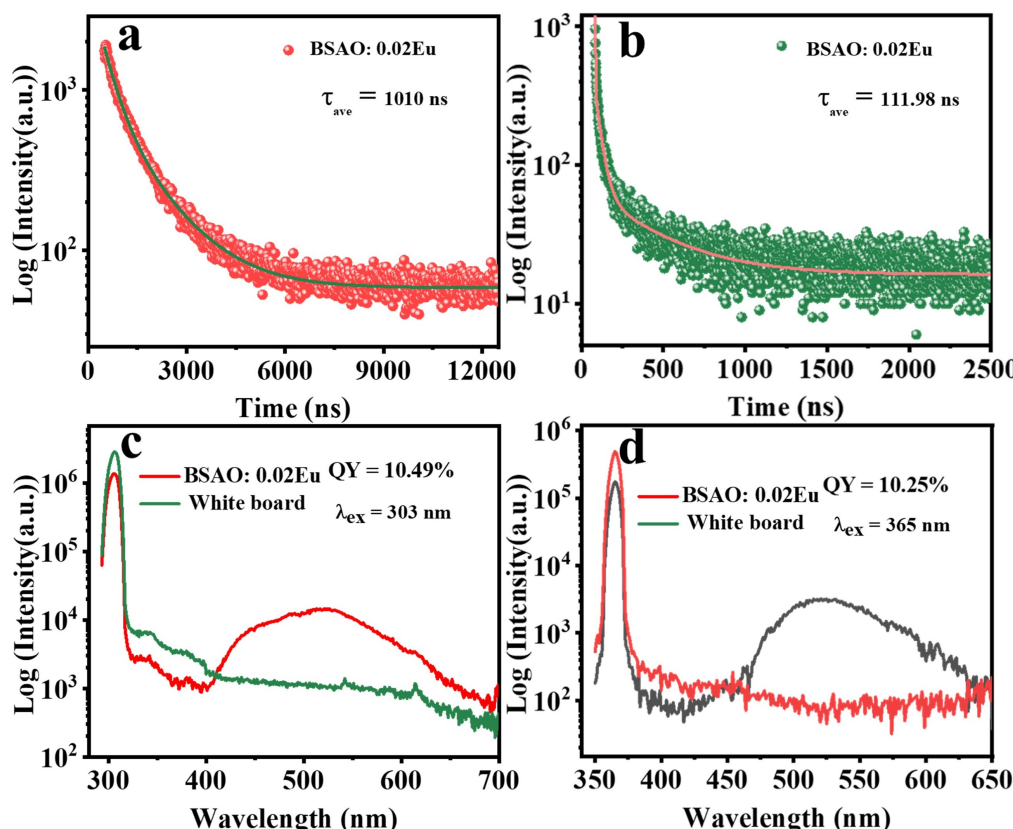


Figure 7. The luminescence decay curves of the BSAO: 0.02 Eu^{2+} ((a) $\lambda_{\text{ex}} = 303 \text{ nm}$, (b) $\lambda_{\text{ex}} = 365 \text{ nm}$) phosphor; (c,d) are the quantum yields of the BSAO: 0.02 Eu^{2+} .

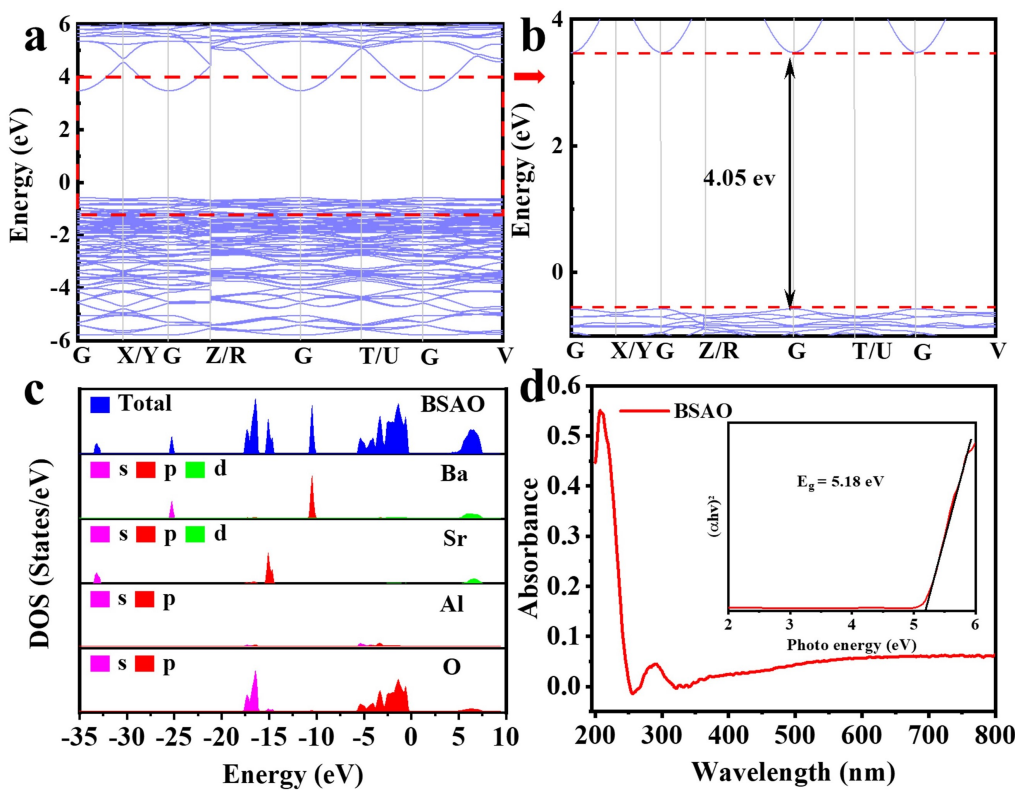


Figure 8. (a,b) Band structure of BSAO; (c) total DOS and partial DOS of BSAO. (d) UV-vis absorption spectra of BSAO host. Inset: The experimental E_g of BSAO host.

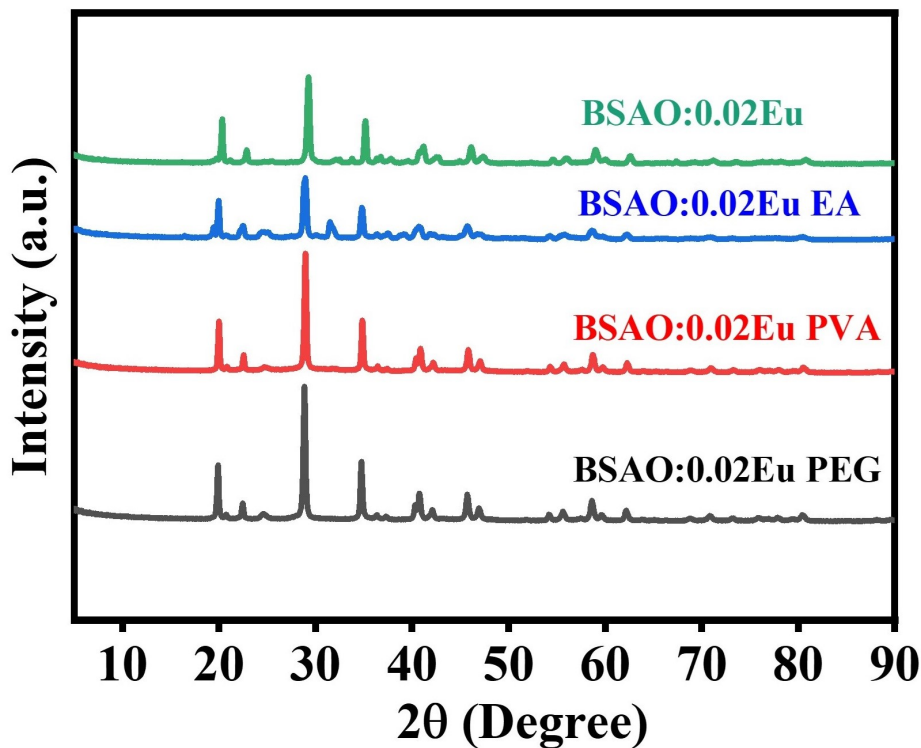


Figure 9. XRD patterns of BSAO: 0.02Eu²⁺ with different surfactants (PEG, PVA, EA).

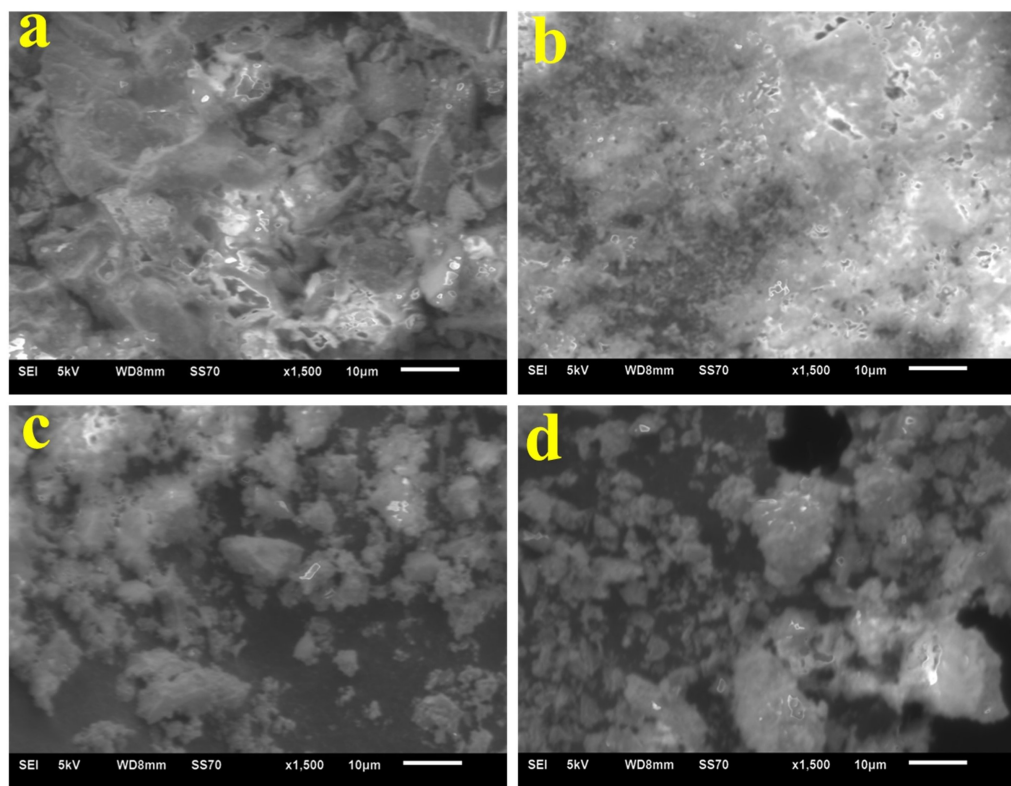


Figure 10. (a) SEM image of BSAO: 0.02Eu^{2+} without surfactant; SEM images of (b) PVA, (c) EA, and (d) PEG were added, respectively.

3.5. Anticounterfeiting Application

To further investigate the anti-counterfeiting properties of phosphors, we fabricate PDMS composite films by embedding optimized Eu^{2+} doped BSAO phosphors in the polydimethylsiloxane (PDMS) polymer matrix. The fabricated luminescent film is well proportioned with flexible performance as presented in Figure 11a. As shown in Figure 11b,c, the BSAO: 0.02Eu^{2+} /PDMS films emit blue and green emissions under 303 nm and 365 nm UV light excitation, respectively. Figure 11d,e show SEM images of the surface and a cross section of the composite film with the letter portion, respectively. It can be seen that the particles are well dispersed in the PDMS substrate. Also, the emission spectra of PDMS film are recorded to confirm that the featured transitions of Eu^{2+} ions are barely affected by the PDMS film as shown in Figure 12. In addition, the good physical and chemical stability and thermal stability of the phosphor-PDMS film are confirmed [52–54]. It means that the resulting luminescent film can meet the requirements of our daily lives and that the performance will not be compromised, even in more extreme environments. Furthermore, fluorescent inks are also prepared for anti-counterfeiting marks and screen-printing applications. As shown in Figure 13a, the ink is coated on the banknote, and the coated area is not significantly different from other parts of the substrate under daylight. However, fluorescence emission can be observed under UV light. Finally, as depicted in Figure 13b, the prepared ink is printed on white paper using screen-printing technology, forming a four-leaf clover pattern. The pattern is almost invisible under visible light but becomes clearly visible under UV light. From the above findings, we suggest that the Eu^{2+} ion-activated BSAO/PDMS composite films and ink are anticipated for high-level anti-counterfeiting applications.

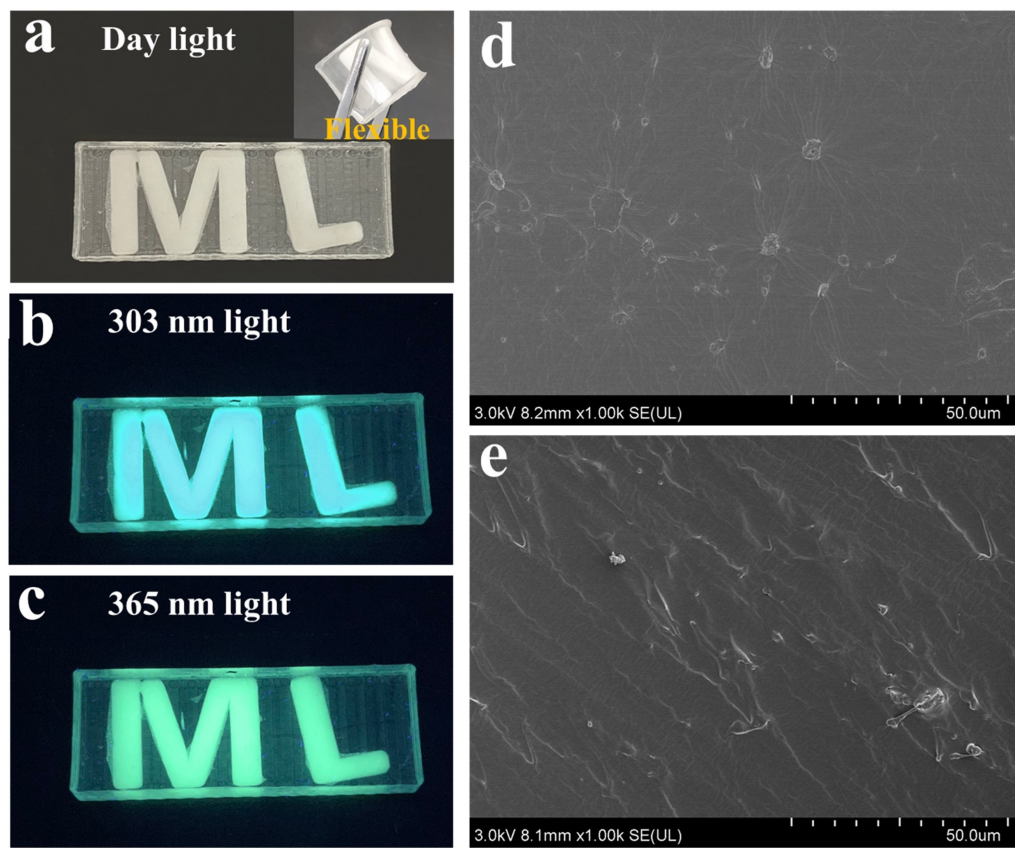


Figure 11. BSAO: 0.02Eu²⁺/PDMS film under (a) daylight, (b) 303 nm light, and (c) 365 nm light; surface (d) and cross section (e) SEM images of the BSAO: 0.02Eu²⁺/PDMS film.

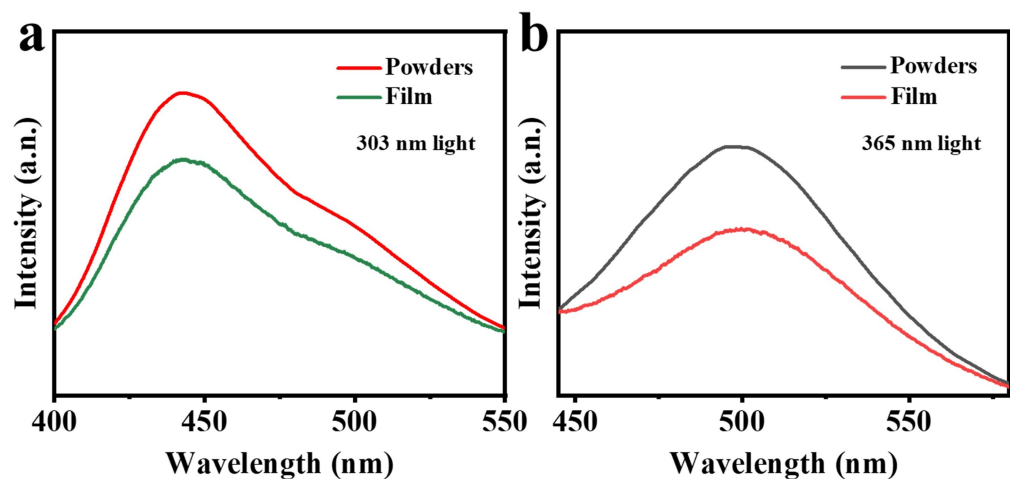


Figure 12. PL emission spectra of the BSAO: 0.02Eu²⁺/PDMS film under (a) 303 nm and (b) 365 nm light irradiations.

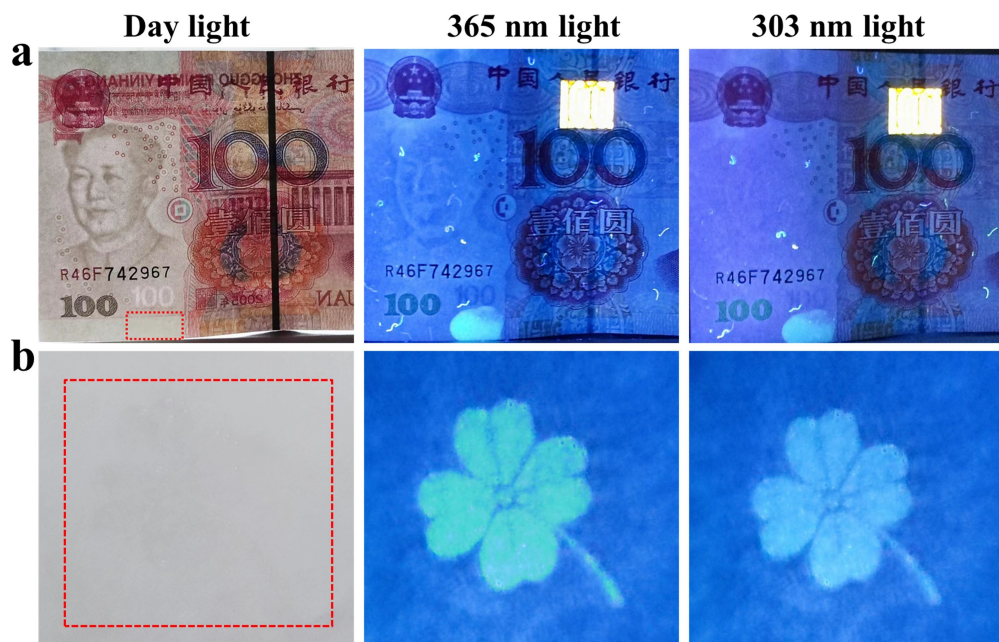


Figure 13. (a) The anti-counterfeiting markings applied on banknotes; (b) the four-leaf clover pattern printed through screen printing.

4. Conclusions

In summary, BSAO: Eu²⁺ phosphors with the hexagonal phase are successfully synthesized via a simple combustion reaction from XRD patterns and EDS spectra. The optical band gap, concentration quenching mechanism, and optimal doping concentration are confirmed. Meanwhile, the optimal BSAO: 0.02Eu²⁺ has a blue-green emission band under the excitation of UV lamps due to the 4f-5d transition of Eu²⁺. In addition, the fluorescence lifetime and the quantum yield are determined as 1010, 111.98 ns, 10.49%, and 10.25%, respectively. Furthermore, an anti-counterfeiting strategy is presented, utilizing phosphors/PDMS films that offer flexibility and exhibit distinct colors when exposed to different UV wavelengths. Finally, by blending the fluorescent powder with ethanol and polyacrylic acid, a transparent ink is prepared, demonstrating the excellent anti-counterfeiting application potential of the fluorescent powder.

Author Contributions: J.W. (Jiao Wu), Q.L. and P.G. designed and carried out the experiment. J.W. (Jiao Wu), J.W. (Jigang Wang), J.H. and W.C. processed the test data. J.Z. provides DFT computational support. With the help of Y.Q., Z.L. and M.C. wrote and completed the paper. All authors have read and agreed to the published version of the manuscript.

Funding: This research is supported by Beijing Natural Science Foundation (No. 2202018), General Project of Beijing Municipal Education Commission Science and Technology Program (No. KM202010015004), Research and development of intelligent packaging for cultural relics (Ed202001), Construction and application transformation of cross media cloud platform for printing and packaging anticounterfeiting and traceability (27170121005), National Natural Science Foundation of China (No. 21604005, Grant No. 52072084), the general project of fundamental research of BIGC (Nos. Ed202208, Eb202001, 20190122041, 22150122042, 22150122034, 27170122012), Initial funding for the Doctoral Program of BIGC (No. 27170121001/002), and the general project of science and technology of Beijing Municipal Education Commission (No. KM202110015008), the Key Area Research and Development Program of Guangdong Province (Grant No. 2020B0101020002), the GBA National Institute for Nanotechnology Innovation (Grant No. 2020GN0106), the National Key R&D Program of China (Grant No. 2021YFC2802000), and National key research and development program (2019YFB1707202).

Institutional Review Board Statement: Not applicable.

Informed Consent Statement: Not applicable.

Data Availability Statement: Research data are not shared.

Conflicts of Interest: The authors declare no conflict of interest.

References

1. Ren, W.; Lin, G.; Clarke, C.; Zhou, J.; Jin, D. Optical nanomaterials and enabling technologies for high-security-level anticounterfeiting. *Adv. Mater.* **2020**, *32*, 1901430. [\[CrossRef\]](#) [\[PubMed\]](#)
2. Liu, F.; Liu, K.; Xie, X.L. Monitoring and limiting deceptive counterfeiting: A two-stage model. *J. Oper. Res. Soc. China* **2016**, *4*, 265–308. [\[CrossRef\]](#)
3. Ofori-Parku, S.S.; Park, S.E. I (Don't) want to consume counterfeit medicines: Exploratory study on the antecedents of consumer attitudes toward counterfeit medicines. *BMC Public Health* **2022**, *22*, 1–13. [\[CrossRef\]](#) [\[PubMed\]](#)
4. Conley, T. Defining and understanding economic globalisation. *Policy Organ. Soc.* **2000**, *19*, 87–115. [\[CrossRef\]](#)
5. Abdollahi, A.; Roghani-Mamaqani, H.; Razavi, B.; Salami-Kalajahi, M. Photoluminescent and chromic nanomaterials for anticounterfeiting technologies: Recent advances and future challenges. *ACS Nano* **2020**, *14*, 14417–14492. [\[CrossRef\]](#) [\[PubMed\]](#)
6. Han, S.; Bae, H.J.; Kim, J.; Shin, S.; Choi, S.E.; Lee, S.H.; Kwon, S.; Park, W. Lithographically encoded polymer microtaggant using high-capacity and error-correctable QR code for anti-counterfeiting of drugs. *Adv. Mater.* **2012**, *24*, 5924–5929. [\[CrossRef\]](#)
7. Li, D.; Tang, L.; Wang, J.; Liu, X.; Ying, Y. Multidimensional SERS barcodes on flexible patterned plasmonic metafilm for anticounterfeiting applications. *Adv. Opt. Mater.* **2016**, *4*, 1475–1480. [\[CrossRef\]](#)
8. Fan, Y.; Zhang, C.; Gao, Z.; Zhou, W.; Hou, Y.; Zhou, Z.; Yao, J.; Zhao, Y.S. Randomly Induced Phase Transformation in Silk Protein-Based Microlaser Arrays for Anticounterfeiting. *Adv. Mater.* **2021**, *33*, 2102586. [\[CrossRef\]](#)
9. Jeon, H.J.; Leem, J.W.; Ji, Y.; Park, S.M.; Park, J.; Kim, K.Y.; Kim, S.W.; Kim, Y.L. Cyber-Physical Watermarking with Inkjet Edible Bioprinting. *Adv. Funct. Mater.* **2022**, *32*, 2112479. [\[CrossRef\]](#)
10. Lv, S.; Shanmugavelu, B.; Wang, Y.; Mao, Q.; Zhao, Y.; Yu, Y.; Hao, J.; Zhang, Q.; Qiu, J.; Zhou, S. Transition metal doped smart glass with pressure and temperature sensitive luminescence. *Adv. Opt. Mater.* **2018**, *6*, 1800881. [\[CrossRef\]](#)
11. Ding, M.; Dong, B.; Lu, Y.; Yang, X.; Yuan, Y.; Bai, W.; Wu, S.; Ji, Z.; Lu, C.; Zhang, K.; et al. Energy manipulation in lanthanide-doped core–shell nanoparticles for tunable dual-mode luminescence toward advanced anti-counterfeiting. *Adv. Mater.* **2020**, *32*, 2002121. [\[CrossRef\]](#)
12. Dorenbos, P. $f \rightarrow d$ transition energies of divalent lanthanides in inorganic compounds. *J. Phys. Condens. Matter* **2003**, *15*, 575. [\[CrossRef\]](#)
13. Liu, Y.; Tu, D.; Zhu, H.; Li, R.; Luo, W.; Chen, X. A strategy to achieve efficient dual-mode luminescence of Eu^{3+} in lanthanides doped multifunctional NaGdF_4 nanocrystals. *Adv. Mater.* **2010**, *22*, 3266–3271. [\[CrossRef\]](#)
14. Dorenbos, P. The $4f^n \leftrightarrow 4f^{n-1}5d$ transitions of the trivalent lanthanides in halogenides and chalcogenides. *J. Lumin.* **2000**, *91*, 91–106. [\[CrossRef\]](#)
15. Li, Q.; Yan, B. Multi-component assembly of luminescent rare earth hybrid materials. *J. Rare Earths* **2019**, *37*, 113–123. [\[CrossRef\]](#)
16. Bai, X.; Cun, Y.; Xu, Z.; Zi, Y.; Haider, A.A.; Ullah, A.; Khan, I.; Qiu, J.; Song, Z.; Yang, Z. Multiple Anti-Counterfeiting and optical storage of reversible dual-mode luminescence modification in photochromic $\text{CaWO}_4: \text{Yb}^{3+}, \text{Er}^{3+}, \text{Bi}^{3+}$ phosphor. *Chem. Eng. J.* **2022**, *429*, 132333. [\[CrossRef\]](#)
17. Li, M.; Yao, W.; Liu, J.; Tian, Q.; Liu, L.; Ding, J.; Xue, Q.; Lu, Q.; Wu, W. Facile synthesis and screen printing of dual-mode luminescent $\text{NaYF}_4: \text{Er}, \text{Yb} (\text{Tm})/\text{carbon dots}$ for anti-counterfeiting applications. *J. Mater. Chem. C* **2017**, *5*, 6512–6520. [\[CrossRef\]](#)
18. Zhang, X.; Qin, X.; Zhang, W. $\text{NaYF}_4: \text{Yb}, \text{Er}$ with N-GQDs mixture: One-pot hydrothermal synthesis and its luminescent film. *Opt. Mater.* **2021**, *114*, 110910. [\[CrossRef\]](#)
19. Pei, P.; Bai, Y.; Su, J.; Yang, Y.; Liu, W. Achieving mechano-upconversion-downshifting-afterglow multimodal luminescence in a lanthanide-doped $\text{LaCaAl}_3\text{O}_7$ phosphor for multidimensional anticounterfeiting. *Sci. China Mater.* **2022**, *65*, 2809–2817. [\[CrossRef\]](#)
20. Sohn, K.S.; Timilsina, S.; Singh, S.P.; Lee, J.W.; Kim, J.S. A mechanoluminescent $\text{ZnS}: \text{Cu}/\text{rhodamine}/\text{SiO}_2/\text{PDMS}$ and piezoresistive CNT/PDMS hybrid sensor: Red-light emission and a standardized strain quantification. *ACS Appl. Mater. Interfaces* **2016**, *8*, 34777–34783. [\[CrossRef\]](#)
21. Hou, Y.F.; Wang, J.; Wang, X.; Liao, Y.P.; Yang, L.; Cai, E.L.; Wang, S.S. Simultaneous measurement of pressure and temperature in seawater with PDMS sealed microfiber Mach-Zehnder interferometer. *J. Light. Technol.* **2020**, *38*, 6412–6421. [\[CrossRef\]](#)
22. Zhao, X.; Ounaies, Z. A facile method to enhance the flexibility and triboelectric output of PDMS using ionic liquid-coated single-wall carbon nanotubes. *Nano Energy* **2022**, *94*, 106908. [\[CrossRef\]](#)
23. Zhao, X.; Li, L.; Li, B.; Zhang, J.; Wang, A. Durable superhydrophobic/superoleophilic PDMS sponges and their applications in selective oil absorption and in plugging oil leakages. *J. Mater. Chem. A* **2014**, *2*, 18281–18287. [\[CrossRef\]](#)
24. Nakauchi, D.; Okada, G.; Kawaguchi, N.; Yanagida, T. Luminescent and scintillation properties of Eu-doped $(\text{Ba}, \text{Sr})\text{Al}_2\text{O}_4$ crystals. *Opt. Mater.* **2019**, *87*, 58–62. [\[CrossRef\]](#)

25. Volhard, M.; Yu, L.; den Engelsen, D.; Fern, G.R.; Ireland, T.G.; Silver, J. Crystal structure, photoluminescence and cathodoluminescence of $\text{Ba}_{1-x}\text{Sr}_x\text{Al}_2\text{O}_4$ doped with Eu^{2+} . *Opt. Mater. Express* **2020**, *10*, 1951–1961. [CrossRef]
26. Rezende, M.V.d.S.; Andrade, A.B.; Valerio, M.E.G.; Montes, P.J.R. The effect of the host composition on the lifetime decay properties of barium/strontium aluminates compounds. *J. Appl. Phys.* **2014**, *115*, 103510. [CrossRef]
27. Kresse, G.; Furthmüller, J. Efficient iterative schemes for ab initio total-energy calculations using a plane-wave basis set. *Phys. Rev. B* **1996**, *54*, 11169. [CrossRef]
28. Kresse, G.; Joubert, D. From ultrasoft pseudopotentials to the projector augmented-wave method. *Phys. Rev. B* **1999**, *59*, 1758. [CrossRef]
29. Perdew, J.P.; Burke, K.; Ernzerhof, M. Generalized gradient approximation made simple. *Phys. Rev. Lett.* **1996**, *77*, 3865. [CrossRef]
30. Blöchl, P.E. Projector augmented-wave method. *Phys. Rev. B* **1994**, *50*, 17953. [CrossRef]
31. Malkamäki, M.; Bos, A.J.; Dorenbos, P.; Lastusaari, M.; Rodrigues, L.C.; Swart, H.C.; Hölsä, J. Persistent luminescence excitation spectroscopy of $\text{BaAl}_2\text{O}_4:\text{Eu}^{2+}, \text{Dy}^{3+}$. *Phys. B Condens. Matter* **2020**, *593*, 411947. [CrossRef]
32. Fukuda, K.; Fukushima, K. Crystal structure of hexagonal SrAl_2O_4 at 1073K. *J. Solid State Chem.* **2005**, *178*, 2709–2714. [CrossRef]
33. Zheng, B.; Fan, J.; Chen, B.; Qin, X.; Wang, J.; Wang, F.; Deng, R.; Liu, X. Rare-earth doping in nanostructured inorganic materials. *Chem. Rev.* **2022**, *122*, 5519–5603. [CrossRef]
34. Wang, Y.; Seto, T.; Ishigaki, K.; Uwatoko, Y.; Xiao, G.; Zou, B.; Li, G.; Tang, Z.; Li, Z.; Wang, Y. Pressure-Driven Eu^{2+} -Doped $\text{BaLi}_2\text{Al}_2\text{Si}_2\text{N}_6$: A New Color Tunable Narrow-Band Emission Phosphor for Spectroscopy and Pressure Sensor Applications. *Adv. Funct. Mater.* **2020**, *30*, 2001384. [CrossRef]
35. Shannon, R.D. Revised effective ionic radii and systematic studies of interatomic distances in halides and chalcogenides. *Acta Crystallogr. Sect. A Cryst. Phys. Diffraction Theory Gen. Crystallogr.* **1976**, *32*, 751–767. [CrossRef]
36. Wang, H.; Li, Z.; Kang, R.; Ji, R.; Wang, Y. $\text{Sr}_2\text{BN}_2\text{Cl}$: Eu^{2+} -Based Narrow-Band Blue-Emitting Phosphor: A Potential Color Converter for Illumination and Displays. *Inorg. Chem.* **2022**, *61*, 18245–18252. [CrossRef] [PubMed]
37. Li, J.; Liu, J.; Ni, Q.; Zhu, Q.; Zeng, Z.; Huo, J.; Long, C.; Wang, Q. Key Role Effect of Samarium in Realizing Zero Thermal Quenching and Achieving a Moisture-Resistant Reddish-Orange Emission in $\text{Ba}_3\text{LaNb}_3\text{O}_{12}:\text{Sm}^{3+}$. *Inorg. Chem.* **2022**, *61*, 17883–17892. [CrossRef]
38. Peng, T.; Yang, H.; Pu, X.; Hu, B.; Jiang, Z.; Yan, C. Combustion synthesis and photoluminescence of $\text{SrAl}_2\text{O}_4:\text{Eu}, \text{Dy}$ phosphor nanoparticles. *Mater. Lett.* **2004**, *58*, 352–356. [CrossRef]
39. Gedekar, K.; Wankhede, S.; Moharil, S.; Belekar, R. d–f luminescence of Ce^{3+} and Eu^{2+} ions in BaAl_2O_4 , SrAl_2O_4 and CaAl_2O_4 phosphors. *J. Adv. Ceram.* **2017**, *6*, 341–350. [CrossRef]
40. Tauc, J. Optical properties and electronic structure of amorphous Ge and Si. *Mater. Res. Bull.* **1968**, *3*, 37–46. [CrossRef]
41. Inaba, K.; Suzuki, S.; Noguchi, Y.; Miyayama, M.; Toda, K.; Sato, M. Metastable $\text{Sr}_{0.5}\text{TaO}_3$ perovskite oxides prepared by nanosheet processing. *Eur. J. Inorg. Chem.* **2008**, *2008*, 5471–5475. [CrossRef]
42. Sangiorgi, N.; Aversa, L.; Tatti, R.; Verucchi, R.; Sanson, A. Spectrophotometric method for optical band gap and electronic transitions determination of semiconductor materials. *Opt. Mater.* **2017**, *64*, 18–25. [CrossRef]
43. Dorenbos, P. Energy of the first $4f^7 \rightarrow 4f^6 5d$ transition of Eu^{2+} in inorganic compounds. *J. Lumin.* **2003**, *104*, 239–260. [CrossRef]
44. Van Uitert, L. Characterization of energy transfer interactions between rare earth ions. *J. Electrochem. Soc.* **1967**, *114*, 1048. [CrossRef]
45. Zhao, K.; Yin, L.; Ma, Z.; Yang, T.; Tang, H.; Cao, P.; Huang, S. Investigation of the solid-solution limit, crystal structure, and thermal quenching mitigation of Sr-substituted $\text{Rb}_2\text{CaP}_2\text{O}_7:\text{Eu}^{2+}$ phosphors for white LED applications. *Inorg. Chem.* **2022**, *61*, 1627–1635. [CrossRef] [PubMed]
46. Zhu, H.; Huang, X.; Li, Y.n.; She, Y.l.; Wang, J.; Wong, W.Y.; Liu, M.; Li, W.; Zhou, Z.; Xia, M. Novel ultra-high-temperature zero-thermal quenching plant-protecting type blue-green dual-emission $\text{KAl}_{11}\text{O}_{17}:\text{Eu}^{2+}, \text{Mn}^{2+}$ phosphors for urban ecological lighting. *J. Mater. Chem. C* **2022**, *10*, 3461–3471. [CrossRef]
47. Pei, P.; Liu, K.; Ju, Z.; Wei, R.; Liu, W. Achieving mechano-upconversion-downshifting-afterglow multimodal luminescence in $\text{Pr}^{3+}/\text{Er}^{3+}$ coactivated $\text{Ba}_2\text{Ga}_2\text{GeO}_7$ for multidimensional anticounterfeiting. *J. Mater. Chem. C* **2022**, *10*, 5240–5248. [CrossRef]
48. Zhang, Y.; Qiao, X.; Wan, J.; Wu, L.A.; Chen, B.; Fan, X. Facile synthesis of monodisperse YAG: Ce^{3+} microspheres with high quantum yield via an epoxide-driven sol-gel route. *J. Mater. Chem. C* **2017**, *5*, 8952–8957. [CrossRef]
49. Cheng, X.; Xie, Z.; Zheng, W.; Li, R.; Deng, Z.; Tu, D.; Shang, X.; Xu, J.; Gong, Z.; Li, X.; et al. Boosting the Self-Trapped Exciton Emission in Alloyed $\text{Cs}_2(\text{Ag}/\text{Na})\text{InCl}_6$ Double Perovskite via Cu^+ Doping. *Adv. Sci.* **2022**, *9*, 2103724. [CrossRef]
50. Locardi, F.; Sartori, E.; Buha, J.; Zito, J.; Prato, M.; Pinchetti, V.; Zaffalon, M.L.; Ferretti, M.; Brovelli, S.; Infante, I.; et al. Emissive Bi-Doped Double Perovskite $\text{Cs}_2\text{Ag}_{1-x}\text{Na}_x\text{InCl}_6$ Nanocrystals. *ACS Energy Lett.* **2019**, *4*, 1976–1982. [CrossRef]
51. Wang, X.; Xu, J.; Yu, J.; Bu, Y.; Marques-Hueso, J.; Yan, X. Morphology control, spectrum modification and extended optical applications of rare earth ion doped phosphors. *Phys. Chem. Chem. Phys.* **2020**, *22*, 15120–15162. [CrossRef] [PubMed]
52. Hua, Y.; Ran, W.; Yu, J.S. Advantageous occupation of europium (III) in the B site of double-perovskite $\text{Ca}_2\text{BB}'\text{O}_6$ ($\text{B} = \text{Y}, \text{Gd}, \text{La}; \text{B}' = \text{Sb}, \text{Nb}$) frameworks for white-light-emitting diodes. *ACS Sustain. Chem. Eng.* **2021**, *9*, 7960–7972. [CrossRef]

53. Patnam, H.; Hussain, S.K.; Yu, J.S. Rare-earth-free Mn⁴⁺ ions activated Ba₂YSbO₆ phosphors for solid-state lighting, flexible display, and anti-counterfeiting applications. *Ceram. Int.* **2023**, *49*, 2967–2977. [[CrossRef](#)]
54. Hua, Y.; Seo, Y.U.; Yun Kim, S.; Kim, H.J.; Su Yu, J. Rare-earth-free Sr₂YSb_{1-x}O₆:xMn⁴⁺: Synthesis, structure, luminescence behavior, thermal stability, and applications. *Chem. Eng. J.* **2021**, *412*, 128633. [[CrossRef](#)]

Disclaimer/Publisher's Note: The statements, opinions and data contained in all publications are solely those of the individual author(s) and contributor(s) and not of MDPI and/or the editor(s). MDPI and/or the editor(s) disclaim responsibility for any injury to people or property resulting from any ideas, methods, instructions or products referred to in the content.